Electrical Power and Energy Systems 122 (2020) 106163

Contents lists available at ScienceDirect

Electrical Power and Energy Systems

journal homepage: www.elsevier.com/locate/ijepes

Effect of frequency-dependent soil parameters on wave propagation and transient behaviors of underground cables

Haoyan Xue[a,*], Akihiro Ametani[b], Yanfei Liu[c,1], Jeewantha De Silva[d,1]

[a] African Office, Global Energy Interconnection Development and Cooperation Organization (GEIDCO), Bole Sub City, Addis Ababa, Ethiopia
[b] The Department of Electrical Engineering, University of Manitoba, 66 Chancellors Cir, Winnipeg, Manitoba R3T 2N2, Canada
[c] Independent Consultant, Ningxia International Language College, Yinchuan, Ningxia, China
[d] Manitoba Hydro International Ltd, 211 Commerce Drive, Winnipeg, Manitoba R3P 1A3, Canada

ARTICLE INFO

Keywords:
Underground cables
Frequency-dependent soil parameter
Earth-return impedance / admittance
Wave propagation
Transient simulations

ABSTRACT

This paper investigates the influence of frequency-dependent (FD) soil parameters in comparison to the constant soil (CS) parameters on wave propagations and transient characteristics of underground cables. Various FD soil models are summarized, and the calculated results of the FD soil parameters are compared with independent measured FD soil data. Longmire / Smith (LS) model is found to show the best agreement with the measured results. The frequency responses of wave propagations on underground cables are studied by the recently proposed extended transmission line (TL) approach together with the CS and the LS FD soil models. Calculated transient responses show more attenuation with a large soil resistivity at 100 Hz in comparison with those with a small soil resistivity at 100 Hz. Further, the transient voltage responses of a cross-bonded cable are compared with the transients solved by the Cable Constants and the existing FD soil routine in an EMT-type simulation tool, and a significant difference is observed.

1. Introduction

Surge analysis in power transmission systems requires accurate calculations of earth-return parameters. The earth-return impedance formula of underground cables was initially developed by Pollaczek [1]. It was further modified by Sunde to include the soil permittivity [2]. Fundamental underground cable modeling and wave propagation characteristics have been investigated by Wedepohl [3]. Also, a systematic study of modal sensitivities of propagation constants on underground cables was performed by Indulkar [4]. Wait and Bridges [5,6] independently derived formulas of the earth-return impedance and admittance for a single underground cable based on an exact expression from electromagnetic theories. More generalized earth-return impedance and admittance formulas for a multi-phase underground cable were derived in [7–11].

Those papers investigated the influence of the constant soil (CS) parameters on wave propagations and transient characteristics of underground cables adopting the derived earth-return impedance and admittance formulas, although the soil parameters are frequency-dependent (FD) as is well-known in [12–19].

Recently, Papadopoulos studied the impact of FD soil properties on electromagnetic field propagations in a single phase underground cable by adopting his earth-return impedance and admittance formulas of underground cables [8,20]. It shows a significant influence of FD soil properties for the wave propagations and transient characteristics of an underground cable. However, the single phase cable investigated in [20] only involves the earth-return mode propagation, and thus the mixed propagation characteristics of a multi-phase underground cable with the CS and the FD soil characteristics require further studies.

Based on the above facts, Section 2 in this paper briefly reviews and summarizes various FD soil models [12–14,18]. The FD soil parameters using values of soil resistivity at 100 Hz based on a logarithmic sampling method [21] are calculated by different FD soil models. The overall characteristics of the FD soil parameters are made clear. Also, some typical calculations [19] of FD soil resistivity and permittivity are performed and compared with the measured results of soil [22,23], and the numerical values are summarized in Appendix A.1.

In Section 3, the series impedance and shunt admittance on the underground cables [20] are calculated by a recently proposed extended transmission line (TL) approach in Appendix A.2 [11] with the CS model and the Longmire / Smith (LS) FD soil model [14] which shows more reasonable agreement with the given measured FD soil data

* Corresponding author.
E-mail address: haoyan-xue@geidco.org (H. Xue).
[1] Co-authors.

https://doi.org/10.1016/j.ijepes.2020.106163
Received 19 February 2020; Received in revised form 26 March 2020; Accepted 2 May 2020

in Appendix A.1. Also, the wave propagation characteristics of the cable are evaluated.

Section 4 performs surge simulations of different modes and presents transient simulations for a cross-bonded cable [24] by adopting the extended TL approach with the CS and the LS soil models. The transient responses of the cross-bonded cable are also compared with the calculated results using the Cable Constants and the existing FD soil routine in an EMT-type simulation tool [25]. Moreover, a flat, vertical and trefoil cable arrangement on the transient responses are studied. Finally, differences of wave propagations and transient characteristics by the extended TL approach, the CS model and the LS FD soil model are thoroughly investigated.

2. Review of FD soil models and comparison of calculated results

2.1. Review of FD soil models

The formulas of FD soil models [12–14,18] are briefly reviewed and summarized in this section. Based on widely measured results of soil, all the formulas are specifically derived for the representations of FD soil electrical parameters which are conductivity and permittivity.

2.1.1. Longmire / Smith (LS) model

By examining the experimental soil data of Scott and Wilkenfeld, Longmire and Smith have derived a universal FD soil model by adopting a curve-matching method [14]. Moreover, the universal soil model is further scaled by adopting the DC conductivity instead of the water content [19], and it gives the following formulas.

$$\sigma(f) = \sigma_{DC} + 2\pi\varepsilon_0 \sum_{i=1}^{13} a_n F_n \frac{\left(\frac{f}{F_n}\right)^2}{1+\left(\frac{f}{F_n}\right)^2} (\mathrm{S/m}) \tag{1}$$

$$\varepsilon_r(f) = \varepsilon_\infty + \sum_{n=1}^{13} \frac{a_n}{1+\left(\frac{f}{F_n}\right)^2} \tag{2}$$

where f is the frequency in Hz and ranges from 100 Hz to 200 MHz, $\sigma(f)$ is the FD soil conductivity, $\varepsilon_r(f)$ is the FD soil relative permittivity, σ_{DC} is the DC soil conductivity in S/m, a_n is the empirical coefficient and is given in Table 1 [14,19], ε_∞ is the high frequency permittivity and is set to 5 [14], ε_0 is the vacuum permittivity and the scaled F_n is given by

$$F_n = F(\sigma_{DC})10^{n-1} \tag{3}$$

with

$$F(\sigma_{DC}) = (125\sigma_{DC})^{0.8312} \tag{4}$$

2.1.2. Alipio / Visacro (AV) model

Based on a large number of field measurements, Alipio and Visacro proposed the formulation to take into account the dispersion of soil frequency dependence by adopting solid physical assumptions [18]. The expressions of the soil frequency dependence are given by [18]

Table 1
The values of Empirical Coefficients for Longmire / Smith Model.

n	1	2	3	4	5
a_n	3.4×10^6	2.74×10^5	2.58×10^4	3.38×10^3	5.26×10^2
n	6	7	8	9	10
a_n	1.33×10^2	2.72×10^1	1.25×10^1	4.8	2.17
n	11	12	13	–	–
a_n	9.8×10^{-1}	3.92×10^{-1}	1.73×10^{-1}	–	–

$$\sigma(f) = \left[\sigma_0 + 1.26\sigma_0^{0.27}\left(\frac{f}{10^6}\right)^\gamma\right]\cdot 10^{-3}(\mathrm{mS/m}) \tag{5}$$

$$\varepsilon_r(f) = \varepsilon_{r\infty} + \frac{1.26\cdot 10^{-3}\tan\left(\frac{\pi\gamma_{av}}{2}\right)\sigma_0^{0.27} f^{\gamma_{av}-1}}{2\pi\varepsilon_0\cdot 10^{6\gamma_{av}}} \tag{6}$$

where f ranges from 100 Hz to 4 MHz, γ_{av} is the empirical coefficient and is set to 0.54p.u. [18], $\varepsilon_{r\infty}$ is the high frequency relative permittivity and is set to 12 [18].

2.1.3. Scott (SC) model

Field and laboratory measurements of various soil samples with different water contents have been performed by Scott, and the following curve-matching expressions of FD soil model are proposed in [12,13].

$$\sigma(f) = 10^K\ (\mathrm{mS/m}) \tag{7}$$

$$\varepsilon_r(f) = 10^D \tag{8}$$

where f ranges from 100 Hz to 1 MHz, the coefficients K and D are given by

$$K = 0.028 + 1.098\log_{10}(\sigma_0) - 0.068\log_{10}(f) + 0.036\log_{10}^2(\sigma_0) - 0.046\log_{10}(f)\log_{10}(\sigma_0) + 0.018\log_{10}^2(f) \tag{9}$$

$$D = 5.491 + 0.946\log_{10}(\sigma_0) - 1.097\log_{10}(f) + 0.069\log_{10}^2(\sigma_0) - 0.114\log_{10}(f)\log_{10}(\sigma_0) + 0.067\log_{10}^2(f) \tag{10}$$

with σ_0 is the soil conductivity at 100 Hz in mS/m.

2.2. Calculated results of FD soil models

Fig. 1 and Fig. 2 show the calculated FD soil resistivities ($1/\sigma(f)$) and FD soil relative permittivities using previously discussed FD soil models.

Based on a logarithmic sampling method in [21], low and high values of the soil resistivity at 100 Hz ($\rho_0 = 1/\sigma_0$) are adopted in the

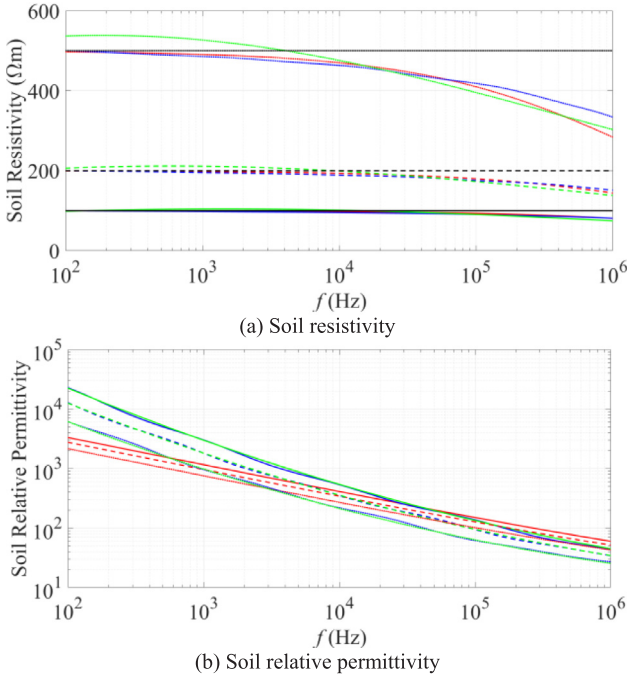

(a) Soil resistivity

(b) Soil relative permittivity

Fig. 1. Calculated results of FD soil parameters, solid line: $\rho_0 = \rho_{cs} = 100$ Ωm, dashed line: $\rho_0 = \rho_{cs} = 200$ Ωm, dotted line: $\rho_0 = \rho_{cs} = 500$ Ωm, black: CS model, blue: LS model, red: AV model, green: SC model.

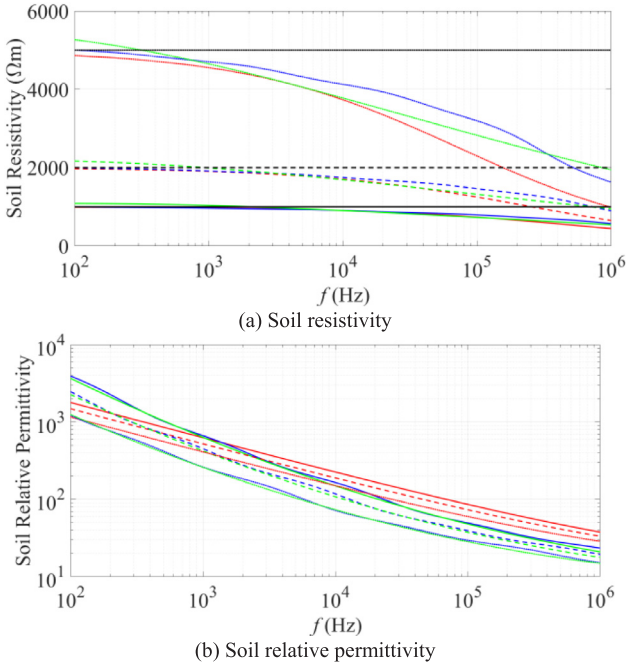

(a) Soil resistivity

(b) Soil relative permittivity

Fig. 2. Calculated results of FD soil parameters, solid line: $\rho_0 = \rho_{cs} = 1000$ Ωm, dashed line: $\rho_0 = \rho_{cs} = 2000$ Ωm, dotted line: $\rho_0 = \rho_{cs} = 5000$ Ωm, black: CS model, blue: LS model, red: AV model, green: SC model.

following calculations. The low values of ρ_0 with 100 Ωm, 200 Ωm and 500 Ωm cover the major surge simulations performed by [8,11]. The high values of ρ_0 with 1000 Ωm, 2000 Ωm and 5000 Ωm can be used to investigate the cable transients for the cases with very large soil resistivity [10]. The CS resistivities ρ_{cs} are also compared with the calculated FD soil resistivities.

The general characteristics are summarized below.

(a) The values of FD soil resistivity and FD soil relative permittivity decrease significantly as frequency increases.
(b) The FD soil relative permittivities show much larger values at a low frequency, i.e. $f < 10$ kHz than that at a high frequency.
(c) As ρ_0 increases, the FD soil relative permittivities decrease.
(d) The FD soil relative permittivities calculated by the LS and SC models have minor differences.
(e) As frequency increases, the differences between the CS resistivities and the FD soil resistivities increase.
(f) The differences between the CS resistivities and the FD soil resistivities are more significant for the large values of ρ_0 and ρ_{cs}.

As shown in Appendix A.1, the FD electrical parameters calculated by the LS, AV and SC models match qualitatively with the independent wide-band measured data of soil in [22,23], and the results of LS model show a better agreement than the other two models. Therefore, the LS model is used to perform frequency and time domain studies in Section 3 and Section 4.

It should be noted that a similar comparison between the parameters evaluated by FD soil models and the independent measured results [22,23] has been performed in [19].

3. Wave propagation characteristics

Fig. 3 illustrates the configuration of a 132 kV cable [24]. The wave propagation characteristics of the cable system in Fig. 3 are investigated based on the extended TL approach (See Appendix A.2), the CS and the LS soil models in this section.

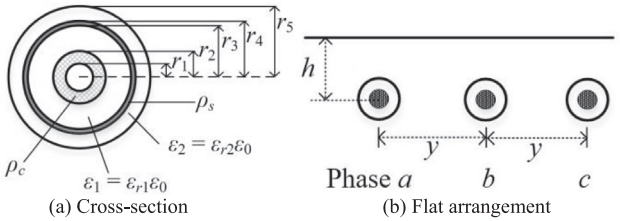

(a) Cross-section (b) Flat arrangement

Fig. 3. 132 kV underground cable configuration, $h = 1$ m, $y = 0.35$ m, $r_1 = 1.03$ cm, $r_2 = 1.9$ cm, $r_3 = 3.45$ cm, $r_4 = 3.85$ cm, $r_5 = 4.25$ cm, $\rho_c = 1.7 \times 10^{-8}$ Ωm, $\rho_s = 2.1 \times 10^{-7}$ Ωm, $\varepsilon_{r1} = 3.5$, $\varepsilon_{r2} = 4$.

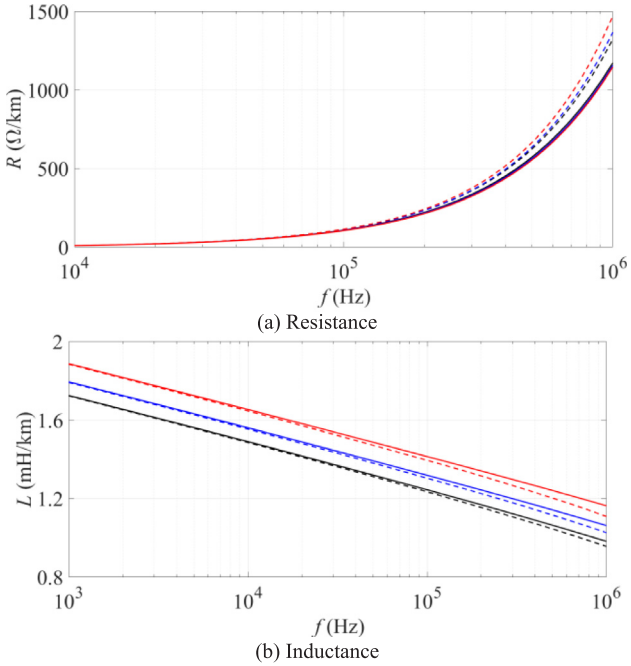

(a) Resistance

(b) Inductance

Fig. 4. Impedance of Phase a - sheath, solid line: CS model, dashed line: LS model, black: $\rho_0 = \rho_{cs} = 100$ Ωm, blue: $\rho_0 = \rho_{cs} = 200$ Ωm and red: $\rho_0 = \rho_{cs} = 500$ Ωm.

3.1. Series impedance and shunt admittance

Figs. 4 to 5 show the impedance of Phase a - sheath calculated by the extended TL approach with the LS model and the corresponding low and high ρ_0 investigated in Section 2. Furthermore, ρ_{cs} of the CS model is set to the same value of ρ_0 and the soil relative permittivity ε_{rcs} of the CS model is assumed to be 1.

If $f < 100$ kHz, no significant difference in the resistance is observed for all the values of soil resistivity and soil models. The inductance increases as ρ_0 and ρ_{cs} increase. Noticeable differences of the impedance are observed between the results evaluated by the CS model and the LS model at a high frequency. The differences become larger for higher values of ρ_0 and ρ_{cs}.

Figs. 6 and 7 illustrate the calculated admittance of Phase a - sheath by the same soil conditions of the impedance. The conductance evaluated by all the values of soil resistivity and soil models increases as frequency increases. The capacitance decreases as frequency increases. The differences of admittance calculated by the CS and the LS models are more visible for the high values of ρ_0 and ρ_{cs}.

A similar trend is observed in the impedance and the admittance of phases b and c, although the results are not shown in this section.

3.2. Modal propagation constants

The modal propagation constants using the same soil models and

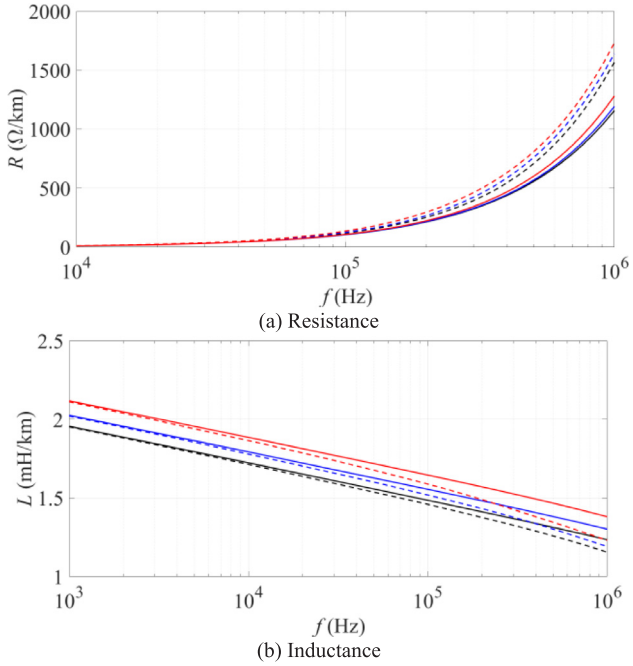

Fig. 5. Impedance of Phase *a* - sheath, solid line: CS model, dashed line: LS model, black: $\rho_0 = \rho_{cs} = 1000$ Ωm, blue: $\rho_0 = \rho_{cs} = 2000$ Ωm and red: $\rho_0 = \rho_{cs} = 5000$ Ωm.

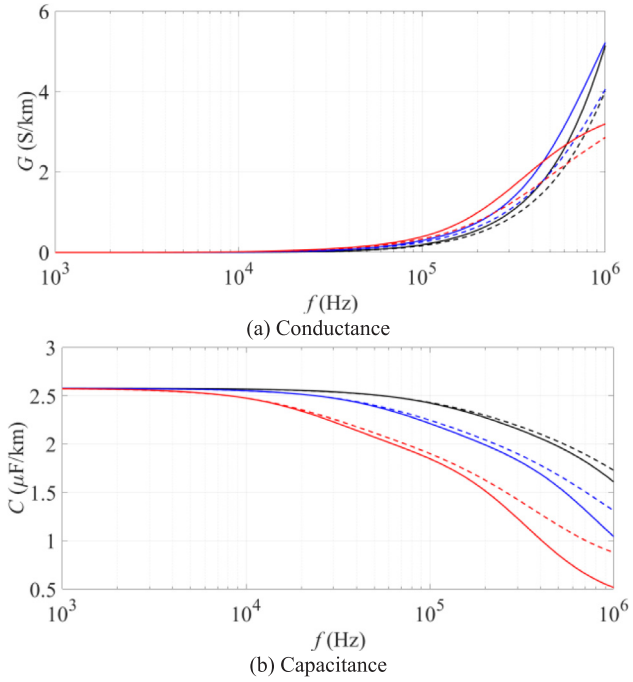

Fig. 6. Admittance of Phase *a* - sheath, solid line: CS model, dashed line: LS model, black: $\rho_0 = \rho_{cs} = 100$ Ωm, blue: $\rho_0 = \rho_{cs} = 200$ Ωm and red: $\rho_0 = \rho_{cs} = 500$ Ωm.

conditions in the previous section are calculated and shown in Figs. 8 and 9. Because the inter-sheath mode 1 shows a minor difference from the inter-sheath mode 2, only the results of the inter-sheath mode 1 are plotted in the figure.

In general, the modal attenuation constants and phase velocities increase as frequency increases. The modal attenuation constants calculated by large values of ρ_0 and ρ_{cs} tend to saturate as frequency increases. The LS model shows a minor influence on the modal

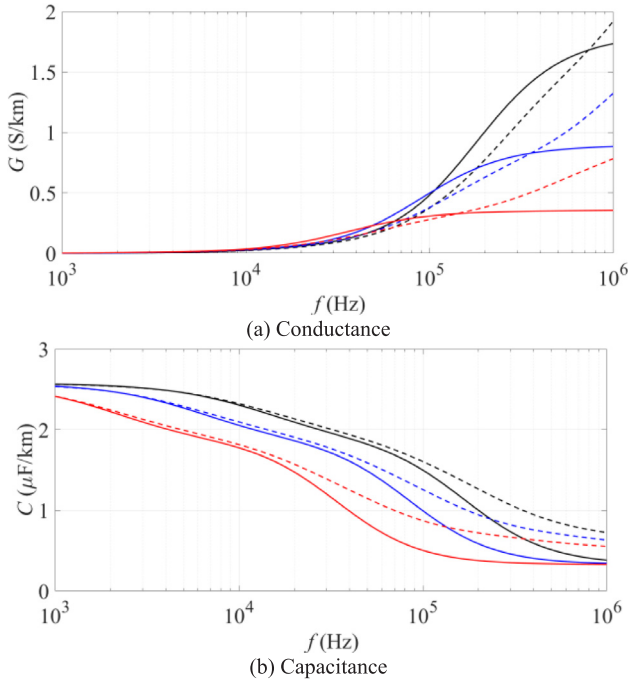

Fig. 7. Admittance of Phase *a* - sheath, solid line: CS model, dashed line: LS model, black: $\rho_0 = \rho_{cs} = 1000$ Ωm, blue: $\rho_0 = \rho_{cs} = 2000$ Ωm and red: $\rho_0 = \rho_{cs} = 5000$ Ωm.

attenuation constants in comparison to the results evaluated by the CS model. However, the modal phase velocities are significantly influenced by the effects of FD soil characteristics in a high frequency region.

The modal propagation constants by the CS model with $\varepsilon_{rcs} = 10$ and 20 are also studied and compared, and no significant difference is observed. Thus, the results are not shown in this paper.

4. Transient responses

4.1. Transient voltage responses for earth-return and inter-sheath modes

Fig. 10 illustrates a cable system, of which the configuration is given in Fig. 3, for the investigations of transient voltage responses. A step voltage source V_s with the amplitude of 1 kV and the rise time t_s of 0.1 μs is applied to the circuit. The existing EMT-type simulation tool [25] is used to perform the simulations by adopting the extended TL approach with the CS and the LS soil models. Also, the values of ρ_0 and ρ_{cs} in Section 2 are used in the simulations.

4.1.1. Inter-sheath mode

Transient voltages on Phase *b* - sheath with different cable lengths are shown in Fig. 11 and Fig. 12 when the step voltage source is applied to the circuit in Fig. 10 (a).

It is clear that the transient sheath voltages calculated by the CS and the LS models with the high values of ρ_0 and ρ_{cs} are damped faster than those by the low values of ρ_0 and ρ_{cs}.

When the cable length is increased to 1 km, a less damping is observed in Fig. 12 (b), especially for $\rho_0 = \rho_{cs} = 5000$ Ωm, in comparison to that for the cable of 0.263 km in Fig. 11 (b). The higher damping for the cable of 0.263 km than that for the cable of 1 km is caused by the higher frequency components involved in the transient responses on the short cable.

The FD soil parameters influence significantly on the transient responses of the cable with the short length and the high values of ρ_0 as shown in Fig. 11 (b).

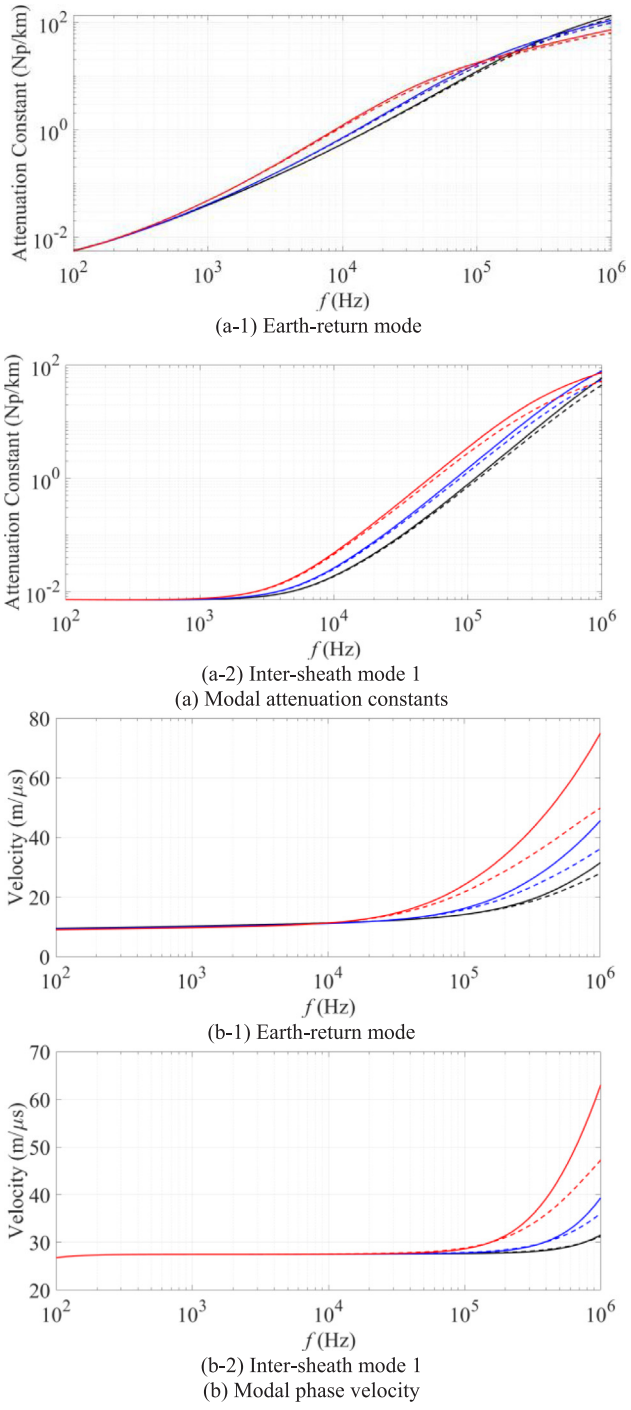

Fig. 8. Modal propagation constants, solid line: CS model, dashed line: LS model, black: $\rho_0 = \rho_{cs} = 100$ Ωm, blue: $\rho_0 = \rho_{cs} = 200$ Ωm and red: $\rho_0 = \rho_{cs} = 500$ Ωm.

4.1.2. Earth-return mode

Fig. 13 and Fig. 14 show Phase *b* - sheath voltages at the receiving end when the step voltage source is applied to the short-circuited three sheaths at the sending end illustrated in Fig. 10 (b).

The transient sheath voltage for the high values of ρ_0 and ρ_{cs} is more attenuated than that for the low values of ρ_0 and ρ_{cs}. This is similar to the transient voltage of the inter-sheath mode shown in Fig. 11 and Fig. 12. Also, the voltage is damped less as the cable length increases.

Again, as illustrated in Fig. 13 (b), the effects of FD soil parameters on the transient voltages are more noticeable for the short cable with the high values of ρ_0.

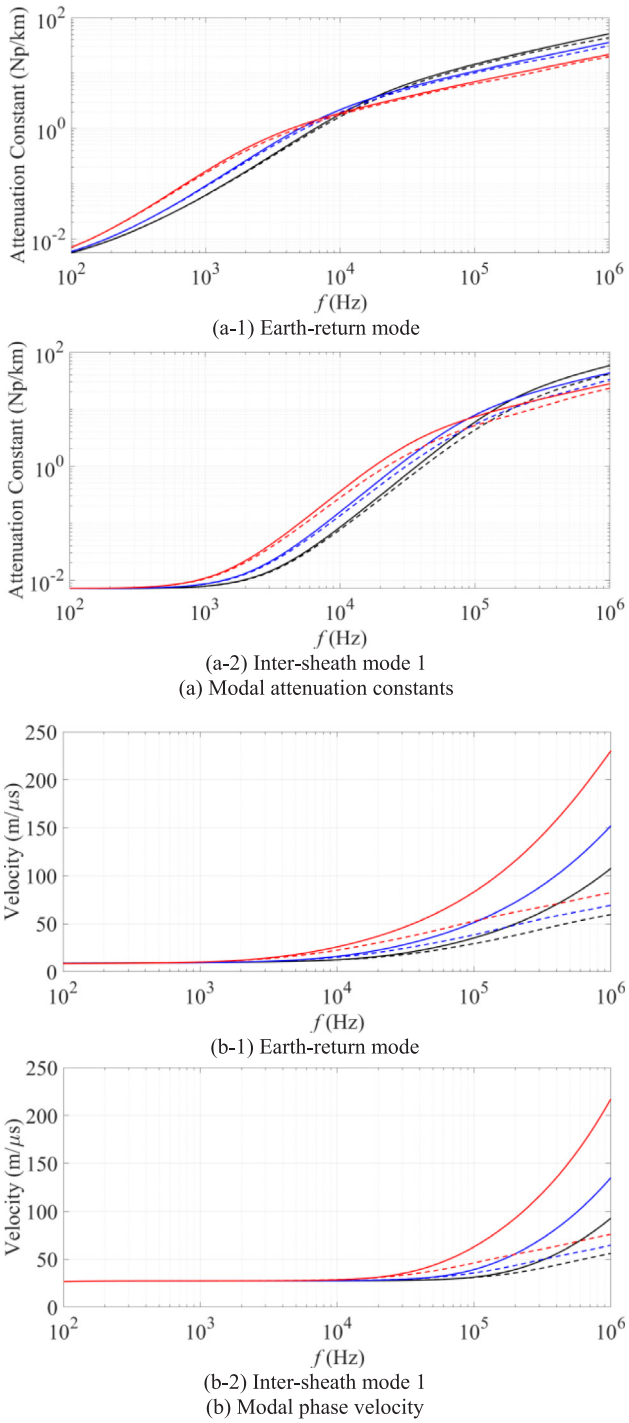

Fig. 9. Modal propagation constants, solid line: CS model, dashed line: LS model, black: $\rho_0 = \rho_{cs} = 1000$ Ωm, blue: $\rho_0 = \rho_{cs} = 2000$ Ωm and red: $\rho_0 = \rho_{cs} = 5000$ Ωm.

4.2. Transient simulations on a cross-bonded cable

Fig. 15 shows a cross-bonded cable composed of three major sections for transient simulations. The cable is energized sequentially by a 110 kV three-phase AC voltage source at the sending end. The closing time of circuit breakers: phases *a* $t = 0$, *b*: $t = 0.1$ and *c*: $t = 0.2$ ms. The bonding scheme of a major section is illustrated in Fig. 15 (b). The length of the major section is 0.788 km. The grounding resistance R_g of each major section is 10 Ω.

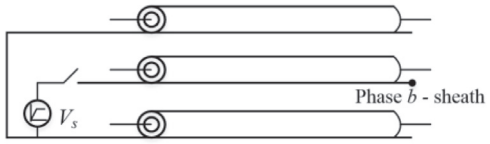

(a) Inter-sheath mode energization

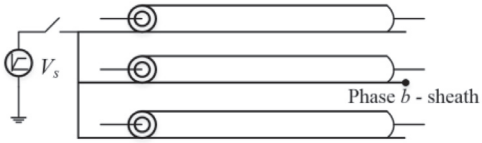

(b) Earth-retun mode energization

Fig. 10. Cable system for transient voltage responses.

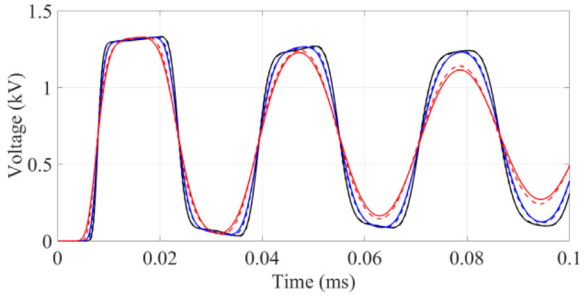

(a) Black: $\rho_0 = \rho_{cs}$ = 100 Ωm, blue: $\rho_0 = \rho_{cs}$ = 200 Ωm and red: $\rho_0 = \rho_{cs}$ = 500 Ωm

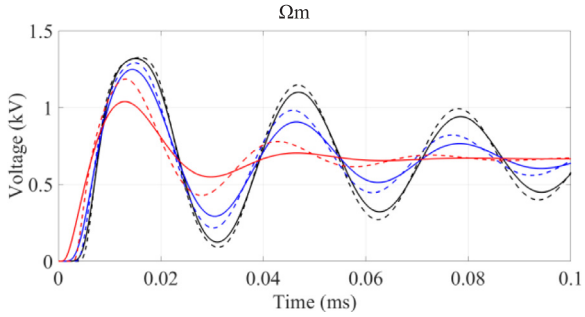

(b) Black: $\rho_0 = \rho_{cs}$ = 1000 Ωm, blue: $\rho_0 = \rho_{cs}$ = 2000 Ωm and red: $\rho_0 = \rho_{cs}$ = 5000 Ωm

Fig. 11. Phase *b* - sheath voltage at the receiving end for inter-sheath mode energization, cable length: 0.263 km, solid line: CS model and dashed line: LS model.

4.2.1. Influence of FD soil parameters

Fig. 16 and Fig. 17 show transient sheath voltages at the receiving end of the cross-bonded cable with a flat arrangement in Fig. 3. The earth-return parameters of the cable are calculated by the extended TL approach with the CS and the LS soil models. Various propagation modes are excited by the sequential energizations of the source. As explained in the previous section, the voltage waveforms show a higher damping, when the resistivity ρ_0 and ρ_{cs} are larger.

As shown in Fig. 16, the FD soil parameters have no noticeable influence on the sheath voltages under the condition of low values of ρ_0 in comparison to the results evaluated by the CS parameters.

However, Fig. 17 shows more important influence of FD soil parameters on the sheath voltages. Taking reference to the sheath voltage evaluated by the CS model, the deviation δ between the peaks of sheath voltages is calculated in the following equation and summarized in Table 2.

$$\delta = \left| \frac{V_{SH-LS} - V_{SH-CS}}{V_{SH-CS}} \right| \times 100\% \tag{11}$$

where V_{SH-LS} and V_{SH-CS} are the peaks of the sheath voltages calculated by the LS and the CS models.

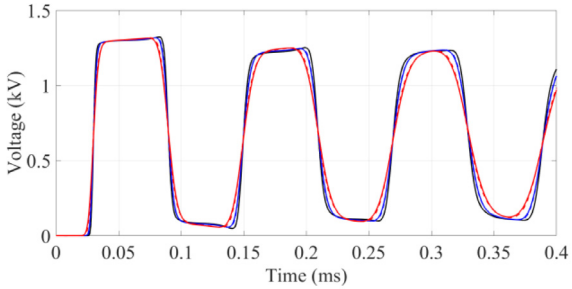

(a) Black: $\rho_0 = \rho_{cs}$ = 100 Ωm, blue: $\rho_0 = \rho_{cs}$ = 200 Ωm and red: $\rho_0 = \rho_{cs}$ = 500 Ωm

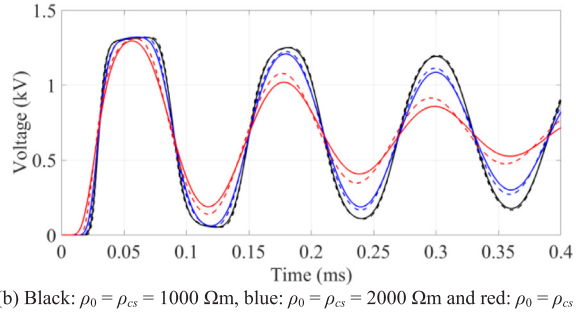

(b) Black: $\rho_0 = \rho_{cs}$ = 1000 Ωm, blue: $\rho_0 = \rho_{cs}$ = 2000 Ωm and red: $\rho_0 = \rho_{cs}$ = 5000 Ωm

Fig. 12. Phase *b* - sheath voltage at the receiving end for inter-sheath mode energization, cable length: 1 km, solid line: CS model and dashed line: LS model.

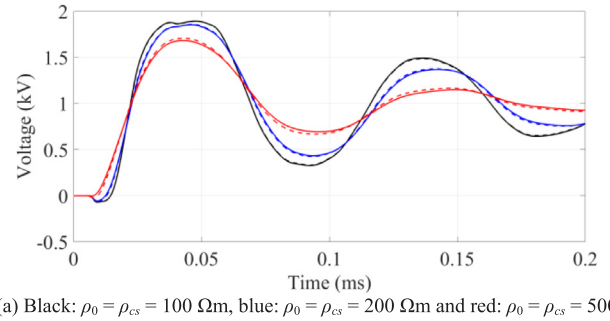

(a) Black: $\rho_0 = \rho_{cs}$ = 100 Ωm, blue: $\rho_0 = \rho_{cs}$ = 200 Ωm and red: $\rho_0 = \rho_{cs}$ = 500 Ωm

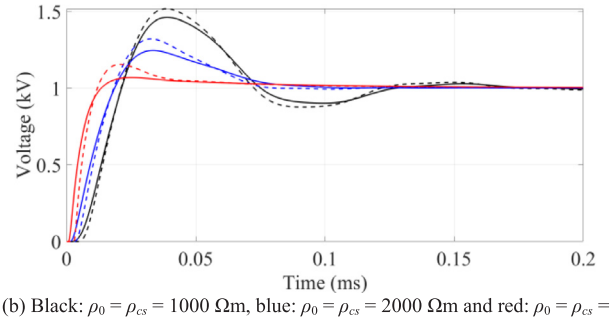

(b) Black: $\rho_0 = \rho_{cs}$ = 1000 Ωm, blue: $\rho_0 = \rho_{cs}$ = 2000 Ωm and red: $\rho_0 = \rho_{cs}$ = 5000 Ωm

Fig. 13. Phase *b* - sheath voltage at the receiving end for earth-return mode energization, cable length: 0.263 km, solid line: CS model and dashed line: LS model.

The largest δ = 11.1% is observed for $\rho_0 = \rho_{cs}$ = 5000 Ωm. The δ increases as ρ_0 and ρ_{cs} increase.

4.2.2. Comparison with results calculated by the existing EMT-type simulation tool

Fig. 18 shows the sheath voltage waveforms calculated by the Cable Constants with an existing FD soil routine in [25], the extended TL approach without the earth-return admittance and the full expression of extended TL approach. Also, the Portela (PR) FD soil model is used to

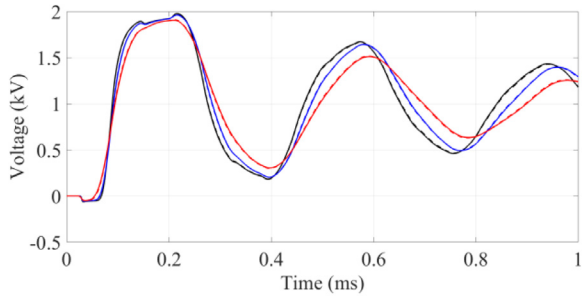

(a) Black: $\rho_0 = \rho_{cs}$ = 100 Ωm, blue: $\rho_0 = \rho_{cs}$ = 200 Ωm and red: $\rho_0 = \rho_{cs}$ = 500 Ωm

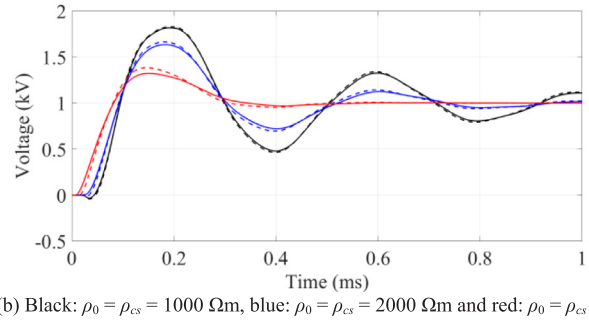

(b) Black: $\rho_0 = \rho_{cs}$ = 1000 Ωm, blue: $\rho_0 = \rho_{cs}$ = 2000 Ωm and red: $\rho_0 = \rho_{cs}$ = 5000 Ωm

Fig. 14. Phase *b* - sheath voltage at the receiving end for earth-return mode energization, cable length: 1 km, solid line: CS model and dashed line: LS model.

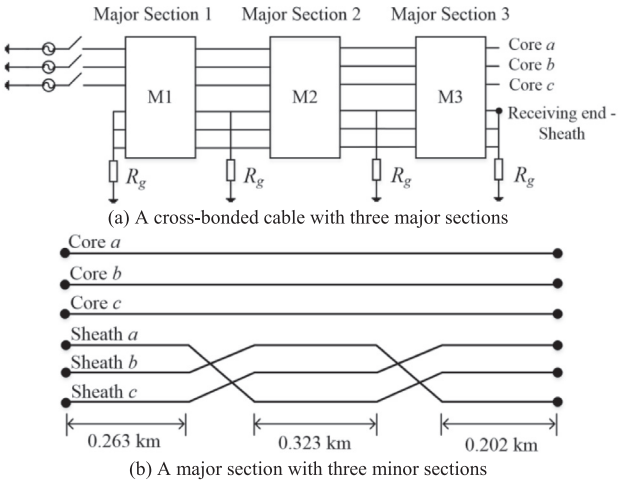

(a) A cross-bonded cable with three major sections

(b) A major section with three minor sections

Fig. 15. Cross-bonded cable system for transient simulations.

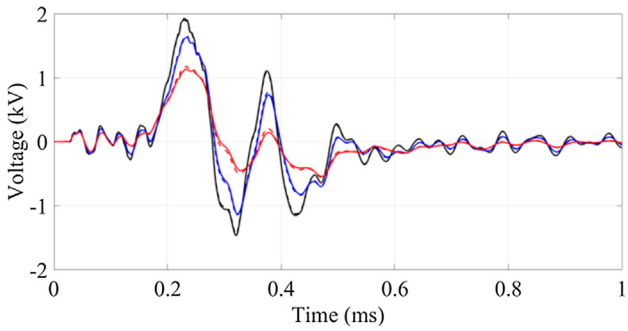

Fig. 16. Sheath voltages at the receiving end of cross-bonded cable in Fig. 3, solid line: CS model, dashed line: LS model, black: $\rho_0 = \rho_{cs}$ = 100 Ωm, blue: $\rho_0 = \rho_{cs}$ = 200 Ωm and red: $\rho_0 = \rho_{cs}$ = 500 Ωm.

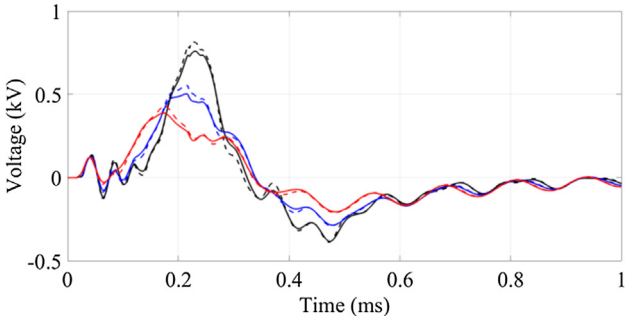

Fig. 17. Sheath voltages at the receiving end of cross-bonded cable in Fig. 3, solid line: CS model, dashed line: LS model, black: $\rho_0 = \rho_{cs}$ = 1000 Ωm, blue: $\rho_0 = \rho_{cs}$ = 2000 Ωm and red: $\rho_0 = \rho_{cs}$ = 5000 Ωm.

Table 2
Deviation of Peak values of Sheath Voltages in Fig. 17.

Soil Resistivity	ρ_0 and ρ_{cs} (Ωm)		
	1000	2000	5000
Deviation δ (%)	7.4%	9.9%	11.1%

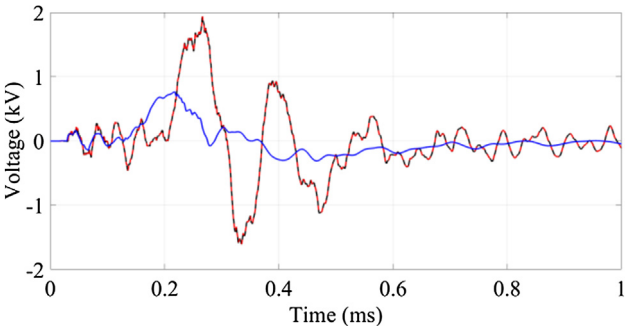

Fig. 18. Sheath voltages at the receiving end of cross-bonded cable in Fig. 3 with ρ_0 = 2000 Ωm, black solid line: Cable Constants and an existing FD soil routine in [25], red dashed line: extended TL approach without earth-return admittance and blue solid line: full expression of extended TL approach.

calculate the sheath voltages in Fig. 18.

It should be noted that the existing method of Cable Constants is defined as the classical TL approach [11] neglecting the earth-return admittance and the soil permittivity in the earth-return impedance.

When the earth-return admittance is neglected, the FD soil permittivity has no significant influence on the sheath voltage, as shown by the black solid line and the red dashed line in Fig. 18. The higher attenuation of the voltage calculated by the full expression of extended TL approach comes from the influence of the earth-return admittance. Thus, the differences are mainly caused by the absence of the earth-return admittance in the classical TL approach.

4.2.3. Influence of cable arrangements

Figs. 19 and 20 show the sheath voltage waveforms at the receiving end of the cross-bonded cable with vertical and trefoil arrangements respectively. The cable data is given in [26]. Only the high values of ρ_0 and ρ_{cs} are considered in the calculations. Also, the deviation δ of Fig. 19 and Fig. 20 is calculated by (11) and summarized in Tables 3 and 4.

It is clear that the trefoil arrangement of the cable shows higher δ for $\rho_0 = \rho_{cs}$ = 1000 and 2000 Ωm than those evaluated by the vertical arrangement of the cable. However, the trefoil arrangement of the cable with $\rho_0 = \rho_{cs}$ = 5000 Ωm shows a smaller δ. In General, the δ is more sensitive to the flat arrangement than the other two arrangements of the

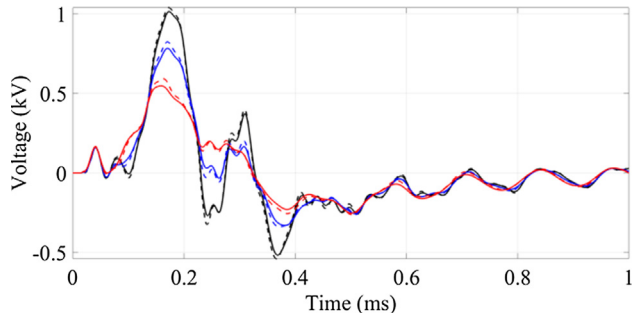

Fig. 19. Sheath voltages at the receiving end of cross-bonded cable in vertical arrangement, solid line: CS model, dashed line: LS model, black: $\rho_0 = \rho_{cs} = 1000$ Ωm, blue: $\rho_0 = \rho_{cs} = 2000$ Ωm and red: $\rho_0 = \rho_{cs} = 5000$ Ωm.

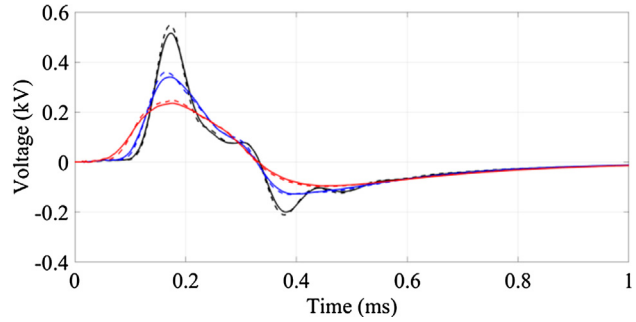

Fig. 20. Sheath voltages at the receiving end of cross-bonded cable in trefoil arrangement, solid line: CS model, dashed line: LS model, black: $\rho_0 = \rho_{cs} = 1000$ Ωm, blue: $\rho_0 = \rho_{cs} = 2000$ Ωm and red: $\rho_0 = \rho_{cs} = 5000$ Ωm.

Table 3
Deviation of Peak values of Sheath Voltages in Fig. 19.

Soil Resistivity	ρ_0 and ρ_{cs} (Ωm)		
	1000	2000	5000
Deviation δ (%)	2.9%	5.1%	9.1%

Table 4
Deviation of Peak values of Sheath Voltages in Fig. 20.

Soil Resistivity	ρ_0 and ρ_{cs} (Ωm)		
	1000	2000	5000
Deviation δ (%)	6.2%	7.5%	4.7%

cable.

5. Conclusions

Existing frequency-dependent (FD) soil models are reviewed and summarized in this paper. A large scale values of soil resistivity at 100 Hz ρ_0 are adopted into the FD soil models for the calculations of FD soil parameters. Also, some typical calculated FD soil parameters are compared with the measured results of the FD soil parameters which are considered to be an independent reference. In general, the FD soil parameters calculated by Longmire / Smith (LS), Scott (SC) and Alipio / Visacro (AV) models agree reasonably well with the reference, and the results of LS model show a better agreement with the reference than the results of SC and AV models.

By adopting the extended TL approach with the constant soil (CS) model and the LS FD soil model, the frequency responses of series impedance, shunt admittance and modal propagation constants of a three phase coaxial cable are investigated. The ρ_0 shows a noticeable influence on the modal propagation constants. The modal attenuation constants and the modal phase velocities evaluated by a large ρ_0 are higher than those calculated by the small ρ_0. In comparison with the results calculated by the CS parameters, the FD soil parameters show significant influences on the impedance and the admittance of the cable at a high frequency, and also more differences can be observed for large values of soil resistivity. The modal phase velocities are more sensitive to the FD soil parameters than the modal attenuation constants.

Transient simulations by different mode energizations on a cross-bonded cable are performed. It becomes clear that the large ρ_0 results in higher damping for the transient voltage waveforms. The voltage responses of the inter-sheath and earth-return modes with a short cable and large values of soil resistivity are significantly influenced by the FD soil parameters. The FD soil parameters show more noticeable influences on the sheath voltage of the cross-bonded cable for large values of soil resistivity. Also, a significant difference of transient voltages is observed between the results calculated by the extended TL approach with the FD soil model and those calculated by Cable Constants and an existing FD soil routine in the EMT-type simulation tool.

CRediT authorship contribution statement

Haoyan Xue: Conceptualization, Methodology, Software, Data curation, Writing - original draft, Investigation. **Akihiro Ametani:** Conceptualization, Supervision, Validation, Writing - review & editing. **Yanfei Liu:** . **Jeewantha De Silva:** .

Declaration of Competing Interest

The authors declare that they have no known competing financial interests or personal relationships that could have appeared to influence the work reported in this paper.

Appendix A

A.1 Calculated results of FD soil models and measured data

The FD soil models discussed in Section 2, the Portela (PR) and the Visacro / Portela (VP) FD soil models are used to calculate the FD resistivities

Table A1
Calculated Resistivity by FD Soil Models with $\rho_0 = 93.2$ Ωm and Measured Data.

Frequency (Hz)	10^2	10^3	10^4	10^5	10^6	10^7
Measured Data (Ωm) [22]	93.2	89.6	87.1	84.7	82.2	74.8
LS (Ωm)	93.2	91.5	89.18	84.77	76.21	56.19
AV (Ωm)	93.06	92.7	91.5	87.57	76.21	52.57
SC (Ωm)	91.41	96.92	94.58	84.96	70.25	53.46
PR (Ωm)	93.12	92.82	91.28	84.2	60.39	24.79
VP (Ωm)	93.2	78.96	66.9	56.68	48.02	40.68

Table A2
Calculated Relative Permittivity by FD Soil Models with ρ_0 = 93.2 Ωm and Measured Data.

Frequency (Hz)	10^2	10^3	10^4	10^5	10^6	10^7
Measured Data [22]	42,500	3820	384	112	20.4	16.0
LS	24,160	3171	556.1	141.4	44.35	21.42
AV	3385	1182	417.5	152.6	60.75	28.91
SC	23,890	3153	566.6	138.6	46.16	20.93
PR	3157	1604	815.1	414.2	210.5	107
VP	13,230	3346	846.4	214.1	54.15	13.7

Table A3
Calculated Resistivity by FD Soil Models with ρ_0 = 198 Ωm and Measured Data.

Frequency (Hz)	10^2	10^3	10^4	10^5	10^6	10^7
Measured Data (Ωm) [22]	198	191	185	180	171	139
LS (Ωm)	198	193.6	187.2	173.9	150	95.74
AV (Ωm)	197.5	196.2	191.8	178.2	142.8	84.63
SC (Ωm)	204.5	209.4	197.4	171.3	136.8	100.6
PR (Ωm)	197.7	196.3	189.5	161.4	91.92	28.85
VP (Ωm)	198	167.8	142.1	120.4	102	86.43

Table A4
Calculated Relative Permittivity by FD Soil Models with ρ_0 = 198 Ωm and Measured Data.

Frequency (Hz)	10^2	10^3	10^4	10^5	10^6	10^7
Measured Data [22]	22,900	2030	194	41.5	18.1	15.4
LS	12,960	1824	354.6	94.41	34.38	17.23
AV	2764	966.2	342.9	126.7	51.78	25.79
SC	12,710	1828	357.9	95.41	34.63	17.11
PR	3157	1604	815.1	414.2	210.5	107
VP	8841	2236	565.6	143.1	36.18	9.152

Table A5
Calculated Resistivity by FD Soil Models with ρ_0 = 296 Ωm and Measured Data.

Frequency (Hz)	10^2	10^3	10^4	10^5	10^6	10^7
Measured Data(Ωm) [22]	296	287	280	275	254	200
LS (Ωm)	296	288.7	277.8	254.9	213.9	127
AV (Ωm)	294.9	292.4	283.8	257.5	195	105.8
SC (Ωm)	311.9	313.6	290.2	247.2	193.8	139.8
PR (Ωm)	295.2	292.2	277.5	221	108.6	30.31
VP (Ωm)	296	250.8	212.5	180	152.5	129.2

Table A6
Calculated Relative Permittivity by FD Soil Models with ρ_0 = 296 Ωm and Measured Data.

Frequency (Hz)	10^2	10^3	10^4	10^5	10^6	10^7
Measured Data [22]	14,100	1210	127	34.4	18.3	15.5
LS	9141	1345	280.7	76.61	30.54	15.56
AV	2481	868.1	308.8	114.9	47.69	24.37
SC	9202	1386	284	79.27	30.12	15.58
PR	3157	1604	815.1	414.2	210.5	107
VP	7130	1803	456.1	115.4	29.18	7.38

Table A7
Calculated Resistivity by FD Soil Models with ρ_0 = 343 Ωm and Measured Data.

Frequency (Hz)	10^2	10^3	10^4	10^5	10^6	10^7
Measured Data (Ωm) [22]	343	330	317	306	282	219
LS (Ωm)	343	334.2	320.9	293.1	243.1	140.5
AV (Ωm)	341.6	338.3	327.2	294.1	217.5	114.3
SC (Ωm)	363.6	363.1	333.7	282.3	219.9	157.6
PR (Ωm)	341.9	337.8	318.3	246.1	114.3	30.7
VP (Ωm)	343	290.5	246.2	208.5	176.7	149.7

Table A8
Calculated Relative Permittivity by FD Soil Models with ρ_0 = 343 Ωm and Measured Data.

Frequency (Hz)	10^2	10^3	10^4	10^5	10^6	10^7
Measured Data [22]	14,600	1430	161	42.1	19	15.9
LS	8096	1213	259.9	71.59	29.42	15.07
AV	2385	834.7	297.3	110.9	46.3	23.89
SC	8195	1255	261.6	74.24	28.68	15.09
PR	3157	1604	815.1	414.2	210.5	107
VP	6589	1667	421.5	106.6	26.97	6.82

Table A9
Calculated Resistivity by FD Soil Models with ρ_0 = 1800 Ωm and Measured Data.

Frequency (Hz)	10^2	10^3	10^4	10^5	10^6	10^7
Measured Data (Ωm) [23]	1800	1600	1500	1400	1000	360
LS (Ωm)	1800	1724	1582	1334	839	337.4
AV (Ωm)	1776	1720	1550	1155	613.3	233.5
SC (Ωm)	1952	1806	1538	1206	869.9	577.8
PR (Ωm)	1772	1667	1280	587.4	156.6	33.14
VP (Ωm)	1800	1525	1292	1095	927.4	785.7

Table A10
Calculated Relative Permittivity by FD Soil Models with ρ_0 = 1800 Ωm and Measured Data.

Frequency (Hz)	10^2	10^3	10^4	10^5	10^6	10^7
Measured Data [23]	19,500	1000	105	55	45	40
LS	2670	482.3	124.6	40.77	19.96	11.2
AV	1528	537.8	194.3	75.22	33.92	19.6
SC	2433	450.1	113.3	38.86	18.14	11.53
PR	3157	1604	815.1	414.2	210.5	107
VP	2714	686.5	173.6	43.92	11.11	2.81

and relative permittivities. The results are compared with the independent measured data [22,23] and shown in Tables A1 to A10.

A.2 Extended TL approach

Based on the extended TL approach [11], the generalized formulas of series impedance and shunt admittance of underground cables are given

$$\mathbf{Z} = \mathbf{Z_i} + \mathbf{Z_e} \tag{A.1}$$

$$\mathbf{Y} = j\omega\mathbf{P}^{-1} \tag{A.2}$$

where $\mathbf{Z_i}$ is the internal impedance of the cable [24], $\mathbf{Z_e}$ is the earth-return impedance matrix of the cable and the potential coefficient matrix $\mathbf{P}$ is defined as

$$\mathbf{P} = \mathbf{P_i} + \mathbf{P_e} \tag{A.3}$$

with $\mathbf{P_i}$ and $\mathbf{P_e}$ are the internal and earth-return potential coefficient matrices of the cable.

The theoretical backgrounds and formulations of $\mathbf{Z_e}$ and $\mathbf{P_e}$ have been thoroughly investigated and given in [11].

References

[1] Pollaczek F. Uber das feld einer unendlich langen wechselstrom durchlossenen einfachleitung. E.N.T 1926;3:339–59.
[2] Sunde ED. Earth conduction effects in transmission systems. New York: Dover; 1968.
[3] Wedepohl LM, Wilcox DJ. Transient analysis of underground power-transmission systems. System-model and wave-propagation characteristics. Proc Inst Electr Eng 1973;120(2):253–60.
[4] Indulkar CS, Kumar P, Kothari DP. Sensitivity analysis of modal quantities for underground cables. IEE Proc C - Generat, Transmiss Distribut 1981;128(4):229–34.
[5] Wait JR. Electromagnetic wave propagation along a buried insulated wire. Can J Phys 1972;50:2402–9.
[6] Bridges G. Transient plane wave coupling to bare and insulated cables buried in a lossy half-space. IEEE Trans Electromag Compat 1995;37:62–70.
[7] Theethayi N, Thottappillil R, Paolone M, Nucci CA, Rachidi F. External impdeance and admittance of buried horizontal wires for transient studies using transmission line analysis. IEEE Trans Dielectr Electr Insulation Jun. 2007;14(3):751–61.
[8] Papadopoulos T, Tsiamitros D, Papagiannis G. Impedances and admittance of underground cables for the homogeneous earth case. IEEE Trans Power Delivery 2010;25:961–9.
[9] Zhang B, Zou J, Du X, Lee J, Ju MN. Ground admittance of an underground insulated conductor and its characteristic in lightning induced disturbance problems. IEEE Trans Electromag Compat 2017;59(3):894–901.
[10] Magalhaes APC, de Barros MTC, Lima ACS. Earth return admittance effect on underground cable system modelling. IEEE Trans Power Delivery 2018;33(2):662–70.
[11] Xue H, Ametani A, Mahseredjian J, Kocar I. Generalized formulation of earth-return impedance / admittance and surge analysis on underground cables. IEEE Trans Power Delivery 2018;33(6):2654–63.
[12] Scott JH. Electrical and magnetic properties of rock and soil. Technical Report, U.S. Geological Survey; 1983.
[13] Scott JH, Carroll RD, Cunningham DR. Dielectric constant and electrical conductivity measurements of moist rock: A new laboratory method. J Geophys Res 1967;72(20):5101–15.
[14] Longmire CL, Smith KS. A universal impedance for soils. Santa Barbara, CA: DNA3788T, Mission Research Corp; 1975.
[15] Portela C. Measurement and modeling of soil electromagnetic behaviour. In: Proc Int Symp EMC, symposium record (Cat. No.99CH36261), vol. 2. Seattle, WA, USA, August 2 - 6, 1999. p. 1004–9.
[16] Portela C, Gertrudes JB, Tavares MC, Pissolato J. Earth conductivity and permittivity data measurements: Influence in transmission line transient performance. Electric Power Syst Res 2006;76:907–15.
[17] Visacro FS, Portela CM. Soil permittivity and conductivity behavior on frequency

range of transient phenomena in electric power systems. In: Proc the Symp High Voltage Eng. Braunschweig, Germany, August 24 – 28; 1987. p. 107–112.
[18] Alipio R, Visacro S. Modeling the frequency dependence of electrical parameters of soil. IEEE Trans Electromagn Compat 2014;56(5):1163–71.
[19] Cavka D, Mora N, Rachidi F. A comparison of frequency-dependent soil models: application to the analysis of grounding systems. IEEE Trans Electromag Compat 2014;56(1):177–87.
[20] Papadopoulos TA, Datsios ZG, Chrysochos AI, Mikropoulos PN, Papagiannis GK. Impact of the frequency-dependent soil electrical properties on the electromagnetic field propagation in underground cables. *Proc International conference on power systems transients*, Perpignan, France, June. 2019.
[21] Ametani A, Imanishi K. Development of exponential Fourier transform and its application to electrical transients. Proc IEE 1979;126(1):51–6.
[22] Bigelow RC, Eberle WR. Empirical predictive curves for resistivity and dielectric constant of earth materials: 100 Hz to 100 MHz. Open-File Report 83-911, U.S. Geological Survey; 1972.
[23] He J, Zeng R, Zhang B. Methodology and technology for power system grounding. Wiley-IEEE Press; 2013.
[24] Ametani A, Ohno T, Nagaoka N. Cable system transients: theory, modeling and simulation. Wiley-IEEE Press; 2015.
[25] PSCAD™/EMTDC™ V5.0, Manitoba Hydro International Ltd., Manitoba, Canada.
[26] Xue H. General formulation and accurate evaluation of earth-return parameters for overhead / underground cables. Ph.D. dissertation, Ecole Polytechnique, University of Montreal., Montreal; 2018.